A new Chemical Lagrangian Model of the Stratosphere (CLaMS) 1. Formulation of advection and mixing

Daniel S. McKenna, Paul Konopka, Jens-Uwe Grooß, Gebhard Günther, and Rolf Müller
Institute for Stratospheric Chemistry (ICG-1), Jülich, Germany

Reinhold Spang[1] and Dirk Offermann
Department of Physics, University of Wuppertal, Wuppertal, Germany

Y. Orsolini
Norwegian Institute for Air Research (NILU), Kjeller, Norway

Received 31 October 2000; revised 8 May 2001; accepted 8 June 2001; published 28 August 2002.

[1] Recent satellite observations and dynamical studies have demonstrated the existence of filamentary structures in chemical tracer fields in the stratosphere. It is also evident that such features are often below the spatial resolution of the highest-resolution Eulerian models that have been used up to the present time. These observations have motivated the development of a novel Chemical Lagranigan Model of the Stratosphere (CLaMS) that is based on a Lagrangian transport of tracers. The description of CLaMS is divided into two parts: Part 1 (this paper) concentrates on the Lagrangian dynamics, i.e., on the calculation of trajectories and on a completely new mixing algorithm based on a dynamically adaptive grid, while part 2 describes the chemical integration and initialization procedure. The mixing of different air masses in CLaMS is driven by the large-scale horizontal flow deformation and takes into account the mass exchange between the nearest neighbors determined by Delaunay triangulation. Here we formulate an isentropic, i.e., two-dimensional version of the model and verify the mixing algorithm using tracer distributions measured during the space shuttle CRISTA-1 experiment where highly resolved stratospheric structures were observed in early November 1994. A comparison of the measured Southern Hemispheric N_2O distribution with CLaMS results allows the intensity of simulated mixing to be optimized. The long-term robustness of the transport scheme is investigated in a case study of the 1996–1997 Northern Hemisphere polar vortex. This study further provides a dynamical framework for investigations of chemical arctic ozone destruction discussed in part 2. *INDEX TERMS:* 0341 Atmospheric Composition and Structure: Middle atmosphere—constituent transport and chemistry (3334); 3334 Meteorology and Atmospheric Dynamics: Middle atmosphere dynamics (0341, 0342); *KEYWORDS:* atmosphere, stratosphere, CLaMS, Lagrangian, tracers

1. Introduction

[2] This paper describes a novel Chemical Lagrangian Model of the Stratosphere (CLaMS) based on a Lagrangian tracer transport. This development has been motivated by recent satellite observations [*Riese et al.*, 1999], in situ measurements [*Tuck et al.*, 1989], and dynamical studies based on such experiments [e.g., *Waugh et al.*, 1997; *Balluch and Haynes*, 1997] that have demonstrated the existence of filamentary structures on a broad range of spatial scales in stratospheric chemical tracer fields. The nonlinearity of most chemical reactions implies that their magnitude will depend on the degree of segregation inherent in filamentary structures. Chemical transport models that do not resolve filamentary structures explicitly or realistically represent their dissipation/mix-down will not simulate nonlinear chemical reactions accurately but may either overestimate or underestimate reaction rates [*Edouard et al.*, 1996; *Searle et al.*, 1998a, 1998b; *Tan et al.*, 1998].

[3] With a Lagrangian approach, one considers an ensemble of air parcels (APs) following the fluid and, consequently, forming a time-dependent irregular grid moving with the fluid elements; by contrast, with a Eulerian approach, one considers a fixed spatial grid through which fluid elements move. An advantage of the Lagrangian approach is the ability to resolve small-scale features, often observed in stratospheric flows as elongated filaments. Filaments form because of the stretching/differential advection of fluid elements in sheared flows with tracer gradients [e.g., *Orsolini et al.*, 1998]. They are often below the resolution of the highest-resolution Eulerian models thus

[1]Now at EOS Space Research Center, University of Leicester, Leicester, England, UK.

0148-0227/02/2000JD000114

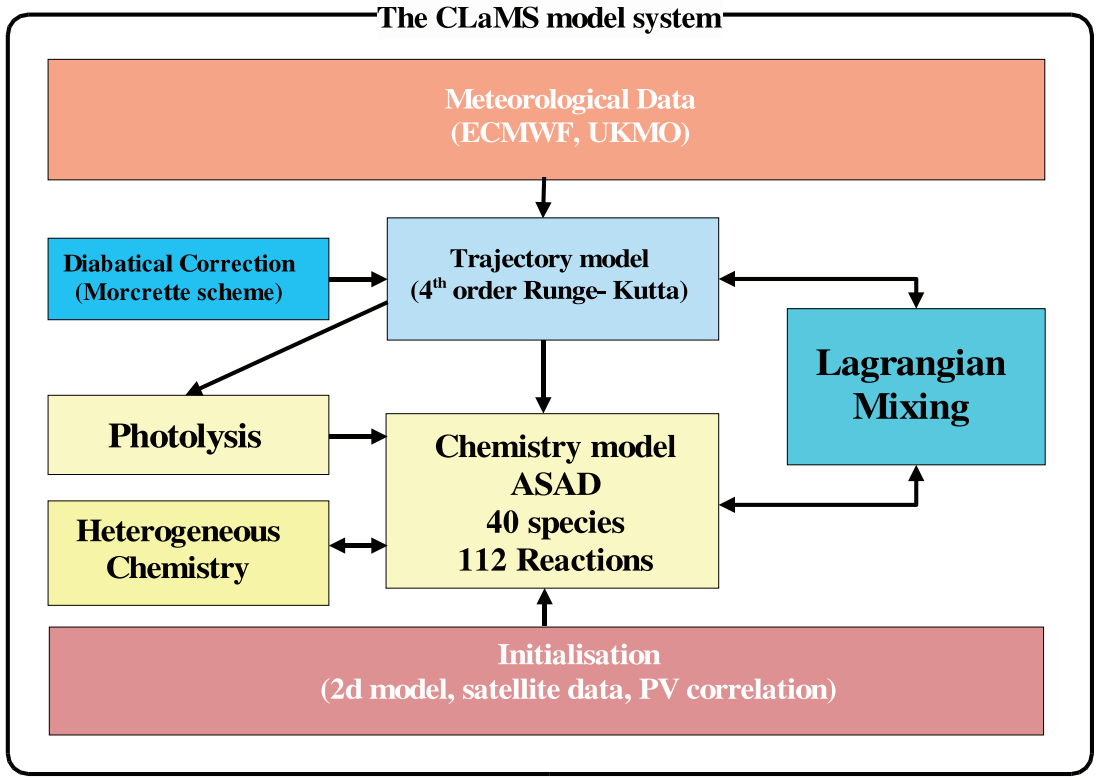

Figure 1. Chemical Lagrangian Model of the Stratosphere (CLaMS) model scheme.

far employed. The reverse-domain-filling technique (RDF) [*Sutton et al.*, 1994] and the contour-advection-with-surgery technique (CAS) [*Norton*, 1994] have shown some skill in reconstructing tracer structures that are not resolved by conventional meteorological analysis or coarse-resolution models [*Plumb et al.*, 1994; *Waugh and Plumb*, 1994; *Appenzeller et al.*, 1996].

[4] One of the shortcomings of a pure Lagrangian transport is the lack of any explicit or implicit mixing between the APs. Thus small (unmixed) structures arise in RDF studies that are not observed even in high-resolution airborne measurements. The "surgery" of the CAS technique overcomes the buildup of small-scale structures by truncating the simulated length scales [*Dritschel*, 1989]. However, neither this first CAS study nor the subsequent applications of CAS have explicitly considered the significance of the surgery as a dissipative process. Additionally, with the RDF technique, unrealistic clustering or dispersion of the advected APs is found after sufficiently large integration times.

[5] The first attempts to simulate stratospheric chemistry along multiple trajectories derived from stratospheric wind analysis were reported by *Austin et al.* [1989]. As computer power has increased with time, it has become possible to simulate stratospheric photochemistry along progressively greater numbers of trajectories [*Lutman et al.*, 1994, 1997]. These techniques avoid the numerical diffusion across the grid box boundaries that inevitably arise with Eulerian schemes [*Rood*, 1987; *Tan et al.*, 1998] but fail to introduce any representation of mixing. More recently, there have been attempts to include mixing and chemistry with multitrajectory simulations. *Collins et al.* [1997] have implemented a hybrid Lagrangian-Eulerian transport scheme that has a parameterization of mixing, as all APs that are advected into a given grid box are mixed together. Naturally, this gridding step introduces numerical diffusion into all grid boxes where more than one AP occurs. *Pierce et al.* [1999] have implemented a stratospheric Lagrangian transport scheme with a mixing parameterization based on the local flow properties [*Fairlie et al.*, 1999]. Although *Fairlie et al.* [1999] provide an objective methodology for mixing APs, undesirable properties near the polar vortex boundaries arise that require an additional assumption that limits AP movement across the polar vortex boundaries. Here we describe the CLaMS Lagrangian transport scheme that avoids the limitations and pitfalls outlined above and that allows the simulation of stratospheric chemistry. On short timescales the APs move on isentropic surfaces, as diabatic processes may be neglected. For longer-term simulations, cross-isentropic transport must be considered [e.g., *Morris et al.*, 1995].

[6] CLaMS comprises three main modules and several submodules (see Figure 1). The main modules are the trajectory module and the mixing module, both described in detail in this paper, and the chemistry module that calculates the change of chemical composition of the APs due to gas phase and heterogeneous chemistry, described by *McKenna et al.* [2002], hereinafter referred to as part 2. Additionally, three preprocessors are employed that process the dynamic input data originating from meteorological data sets, calculate diabatic ascent and descent rates, and initialize the positions of the APs and their chemical composition (also described in part 2). We test the mixing algorithm in an isentropic formulation, using tracer distributions obtained from the CRISTA-1 satellite instrument [*Offermann et al.*, 1999] and check the robustness of the transport

in a long-term study of the 1996–1997 Northern Hemisphere polar vortex. This study provides a dynamical framework for the investigation of winter 1996–1997 Arctic ozone loss discussed in part 2.

2. Lagrangian Transport

2.1. Motivation

[7] Consider an idealized stratosphere with pure isentropic flow and planetary and synoptic-scale disturbances on a zonal flow. Furthermore, consider an idealized passive tracer that has a strong meridional gradient but is zonally symmetric. The action of the large-scale zonal flow will be to move this distribution without disturbing the meridional gradient. However, planetary and synoptic-scale disturbances will typically deform the zonally symmetric distribution [*McIntyre and Palmer*, 1983] and thereby create characteristic elongated streamers/filaments [*Orsolini*, 1995] or cat's eyes [*Ngan and Shepherd*, 1999a, 1999b].

[8] Owing to the stable stratification of the stratosphere, vertical turbulence is weak [e.g., *Woodman and Rastogi*, 1984], while the large-scale horizontal flow consists of an irregular distribution of cyclonic and anticyclonic regions that will give rise to the chaotic advection of tracers [*Lorenz*, 1963]. Thus filaments tend to form two-dimensional (2-D) fractal structures that dissipate by horizontal scale collapse.

[9] This filamentation and scale collapse whereby filaments become progressively longer and thinner will continue until either molecular diffusion or localized and intermittent patches of small-scale turbulence destroy any residual compositional structure. However, atmospheric flow is not uniformly dissipative, so that scale collapse only occurs intermittently in regions with variable shear rates.

[10] Motivated by these properties of the stratospheric flow, we describe in sections 2.2 and 2.3 an isentropic Lagrangian transport scheme with the following properties: (1) the ability to represent the scale collapse associated with 2-D turbulent flow and (2) mixing rates that depend on the evolving flow pattern and are smallest (greatest) when the deformation rate during a time step Δt is smallest (greatest).

2.2. Trajectory Advection

[11] Air motion trajectories are calculated with a scheme provided by R. Swinbank (personal communication, 1993) and described by *Sutton et al.* [1994] using a fourth-order Runge-Kutta scheme with a 30-min time step. Wind velocities at the AP locations are linearly interpolated from the adjacent grid points. Between 72°N and 72°S a spherical coordinate system is used, while poleward of those latitudes a polar stereographic coordinate system is used to avoid numerical problems near the poles.

[12] Wind fields are normally taken from the United Kingdom Meteorological Office (UKMO) Stratosphere-Troposphere Data Assimilation System, although any suitable set of meteorological fields can be used. The UKMO data sets have a meridional and zonal resolution of 2.5° and 3.75°, respectively. There are 22 quasilogarithmically spaced levels between 1000 and 0.316 hPa. Analyses are available for 1200 UT each day.

[13] The trajectory scheme is run with 2-D winds interpolated onto isentropic levels. As discussed in section 1, the assumption of isentropic motion is valid only for restricted timescales. For long-term calculations, cross-isentropic transport must be taken into account. The "vertical" motion of an AP in the isentropic system, the diabatic velocity $\dot{\theta}$, is the material change with time of the potential temperature θ along the path of the APs. Thermal radiation and solar absorption are the principle sources of diabatic change in the stratosphere. To confirm the validity of the isentropic approximations used here and in part 2, we use an improved, numerically more efficient version [*Zhong and Haigh*, 1995] of the Morcrette radiation scheme [*Morcrette*, 1991] originally developed for use in the European Centre for Medium-Range Weather Forecasts (ECMWF) operational model.

2.3. A Dynamically Adaptive Grid (DAG) and Implications for Air Parcel Mixing

[14] The positions of a quasiuniformly spaced ensemble of APs define a quasiuniform grid (i.e., where the nearest-neighbor separations are approximately constant). From these grid point positions, APs are advected during a time step Δt to new positions according to the advective procedure described in section 2.2. After each advection step the grid of AP positions is deformed, and for sufficiently large values of Δt, clustering or dispersion of the initially quasiuniform distribution of grid points occurs.

[15] To determine deformed grid regions, the nearest neighbors (NNs) of the initially quasiuniform grid are found by applying the Delaunay triangulation technique [e.g., *Preparata and Shamos*, 1985]. This method is based on the convex hull algorithm [*Barber et al.*, 1996] for which the computational costs scale as $n \log n$, where n is the number of grid points.

[16] Clusters and voids (i.e., areas with sparse grid-point coverage) are eliminated by applying a dynamically adaptive grid algorithm (see Figure 2) and thereby regenerating a quasiuniform grid-point distribution. This algorithm is applied only when one of the separation criteria described below has been satisfied. Prior to an advection step, NN relationships are determined by Delaunay triangulation. The distances between any given grid point and its former NN are calculated after each advection step. If the separation between it and one of its former NNs exceeds a critical distance r_+^c, a new grid point is inserted midway between the two points (e.g., grid points A and B in Figure 2). To maintain the density of grid points below a given threshold, the new NN relationships are determined and NN separations are calculated; all grid points with distances below the critical distance r_-^c are merged into a new grid point midway between the grid points, and the original grid points are removed (e.g., points A and C in Figure 2). The chemical properties of the new AP associated with each new grid point are initialized with the mean properties of the APs that correspond to the grid points contributing to the calculation of the position of the new grid point.

[17] To link $r_\pm^c$ to the flow deformation during the time step Δt, we introduce the finite-time Lyapunov exponent λ, (hereinafter referred to as Lyapunov exponent λ). Consider a grid point surrounded by a small circle of radius r_0. After a time Δt and for sufficiently small values of r_0, the circle is deformed into an ellipse with minor and major axes r_- and

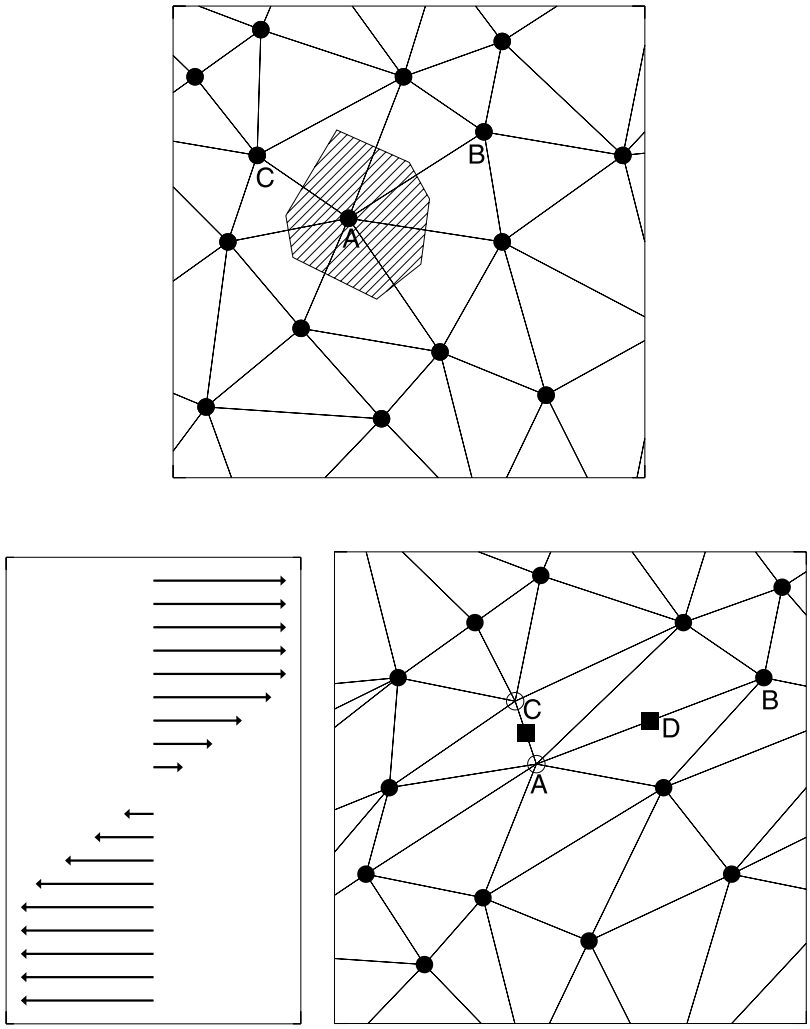

Figure 2. Dynamically adaptive grid algorithm applied on a 2-D quasiuniform distribution of grid points. (top) Initial quasiuniform distribution of grid points denoted by circles. Hatched area defines the Voronoi polygon of a given grid point; that is, all locations within this polygon area are closer to the given grid point than to any other grid point. Grid points that share a polygon side with the hatched polygon are nearest neighbors (NN) of the given grid point. Using Delaunay triangulation, NN of all grid points are simultaneously determined. (bottom) A sheared flow that deforms the ensemble of grid points during an advection step Δt. Thus, for example, the relative distances of the given grid point A to its NN change due to the flow-induced deformation; some grid points like B move further away while some like C move closer. If the distance AB exceeds a critical maximum separation r_+^c, then a new grid point D is inserted midway between A and B (insertion); conversely, if the distance AC falls below a critical minimum separation r_-^c, then grid points A and C are removed and a new grid point is introduced midway between the positions of A and C (merging). Insertion increases the number of grid points by unity, while merging reduces the number of grid points by unity. This procedure will tend to restore grid quasiuniformity.

r_+ (see Figure 3). By definition, the mean logarithmic expansion rate of the principal axes is the Lyapunov exponent [*Geist et al.*, 1990]. Thus

$$\lambda_\pm = \pm\frac{1}{\Delta t}\ln\frac{r_\pm}{r_0}. \tag{1}$$

For incompressible flow, the area of the ellipse is conserved, and $r_-r_+ = r_0^2$. Thus the relation $\lambda_+ = \lambda_-$ holds and, consequently, both the elongation and the contraction rates of the ellipse can be expressed in terms of a single Lyapunov exponent, i.e.,

$$r_\pm/r_0 = \exp(\pm\lambda\Delta t). \tag{2}$$

Using (2), we extend the adaptive grid procedure and link it to the integral deformation in the flow during the time step Δt by relating the individual critical distances r_-^c and r_+^c to a single critical Lyapunov exponent λ_c, through

$$r_\pm^c = r_0\,\exp(\pm\lambda_c\Delta t). \tag{3}$$

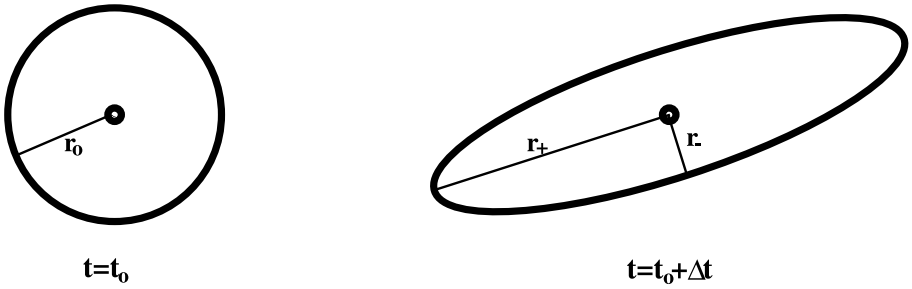

Figure 3. Deformation of a small circle with radius r_0 in a 2-D flow. For sufficiently small values of r_0 and time step Δt the resulting deformation can be approximated by an ellipse with minor and major axes r_- and r_+.

Given a quasiuniform grid distribution, after one time step, certain regions of the grid will be deformed. The adaptation procedure defined above is applied to this deformed grid where r_-^c and r_+^c now been defined through (3) from a single critical Lyapunov exponent λ_c. Note that after determining r_-^c and r_+^c once at the beginning of any given calculation, no further use is made of the critical Lyapunov exponent; adaptation is only invoked when the separation criteria defined by $r_\pm^c$ have been met. Thus the adaptation procedure is controlled in the λ space by choosing a critical Lyapunov exponent λ_c and is carried out in the r space using the corresponding critical radii $r_\pm^c$. By avoiding the calculation of Lyapunov exponents for each grid point, one makes a substantial computational saving.

[18] For special idealized flow configurations, one can link the Lyapunov exponent describing the integral deformation over a time step Δt with the instantaneous (Eulerian) flow properties as the horizontal strain s_h or shear rate s_t. This may be instructive because s_h or s_t are widely used in order to describe the (local) deformation properties of the arbitrary 2-D flow, especially those of the meteorological winds.

[19] In Appendix A we show that in a uniformly sheared 2-D flow with a shear rate s_h, the major/minor axes $r_\pm$ of the deformation ellipse are given by

$$r_\pm^2/r_0^2 = 1 \pm s_h \Delta t \tan^{-/+1}\phi \qquad \tan 2\phi = 2/s_h \Delta t, \tag{4}$$

while, for a pure 2-D strain flow with the velocity field given by $u = s_t y/2$ and $v = s_t x/2$, the major/minor axes $r_\pm$ of the deformation ellipse are given by

$$r_\pm^2/r_0^2 = \exp(\pm s_t \Delta t). \tag{5}$$

Shear s_h and strain s_t deform a unit circle in the same way (up to a solid body rotation) if $\exp(s_t \Delta t) = 1 + s_h \Delta t \tan^{-1}\phi$.

[20] The Lyapunov exponent λ and the local straining rate s_t are simply related by $\lambda = s_t/2$. In the limits of $s_t \Delta t \ll 1$ and $s_h \Delta t \ll 1$ strain and shear, $s_h = s_t$. Furthermore, in a uniformly sheared 2-D flow with sufficiently high shear rates s_h, r_+ and r_- point along and across the wind direction, respectively (for details see Appendix A). In section 2.4 we show in a case study how the adaptation procedure is driven by the integral deformation of the flow quantified by λ and how this integral property can be approximated by the instantaneous shear rate.

[21] Thus, when considering the process as an adaptive gridding procedure, the interpolation of the irregular grid points that correspond to the APs inevitably leads to mixing that can be seen as analogous to the "numerical diffusion" in Eulerian transport schemes. However, in the dynamically adaptive grid (DAG) procedure, mixing only occurs in regions where the flow properties imply high integral deformation rates with $\lambda > \lambda_c$. Typically, the magnitude of grid-point diffusion arising from interpolation between grid points separated by a distance r and for a time step Δt may be approximated by $r^2/4\Delta t$. Thus the magnitude of the equivalent diffusive mixing may be related to the adaptive grid parameters through

$$D_\pm(\lambda) \approx \frac{r_\pm^2}{4\Delta t} = \frac{r_0^2}{4\Delta t}\exp(\pm 2\lambda \Delta t), \tag{6}$$

where D_+ and D_- estimate the magnitude of diffusion equivalent to the mixing resulting from inserting ($r > r_c^+$) and merging ($r < r_c^-$) of APs, respectively. For arbitrary points on the deformation ellipse, the equivalent diffusion varies between D_- and D_+. In flows dominated by the horizontal shear with $\lambda \Delta t$ sufficiently large, D_+ and D_- correspond to diffusion coefficients along and across the local wind direction, respectively. In Appendix B the magnitude of the equivalent diffusivity estimated from (6) is discussed both in λ space and in r space. In addition, we check the validity of (6) using analytical solutions.

[22] The positive definiteness of this transport scheme is ensured by the linear interpolations used to initialize new AP mixing ratios. (By contrast, most Eulerian transport schemes require additional measures to avoid negative concentrations.) The total mass m of a passive tracer for a given model simulation is defined as

$$m = \sum_{i=1}^{n} c_i V_i, \tag{7}$$

where c_i is the concentration and V_i is the volume of the ith AP. In the 2-D simulations the V_i are equivalent to the areas A_i of the Voronoi polygons (Figure 2) corresponding to the ith AP. The magnitude of fluctuations of m (here calculated for CH_4 distribution) that depends on the model resolution does not exceed 0.8% for the low-resolution studies (r_0 = 200 km) and is <0.3% for the high-resolution simulations (r_0 = 60 km) after 45 days of integration.

[23] Thus we have a scheme that formally satisfies the criteria set out in the initial motivation.

1. The separation criterion (equation (3)) permits structure on a scale of order $\exp(-\lambda_c \Delta t)$ smaller than the initial grid resolution r_0 to be resolved. Thus the scheme allows scale collapse to be simulated down to ~20 km when the initial resolution r_0 is on the order of 60 km.

2. The Lyapunov exponents λ vary according to the deformation of an adjacent group of particles in the flow. Thus mixing based on the critical Lyapunov exponent λ_c will be dependent on the integral deformation in the flow.

3. When the separation criterion r_c^+ and r_c^- are satisfied, mixing occurs. The relationship between λ and equivalent diffusivity indicates that mixing will be most intense in regions where deformation is greatest.

[24] Having demonstrated that the mixing algorithm referenced above satisfies the criteria outlined in the motivation, we go on to show in sections 2.4 and 2.5 that the algorithm also gives reasonable qualitative and quantitative results when compared with observations.

2.4. Mixing at the Edge of the Polar Vortex

[25] In order to illustrate the theoretical concepts discussed in section 2.3, we consider a particular case of the horizontal transport near the edge of the North Polar stratospheric vortex. The initial positions of an ensemble of roughly 50,000 APs at $\theta = 475$ K were defined so that their mean separation r_0 was roughly 60 km. Using UKMO wind fields for 15 March 1997, 1200 UTC, the local shear rate s_h defined as the isentropic cross-wind gradient was calculated (Figure 4, top). Figure 4 (bottom) shows the Lyapunov exponent λ calculation for each grid point after one advection step $\Delta t =$ 24 hours. The Lyapunov exponent λ is estimated from the largest relative change of the distance between a given grid point and its NN. Note that the horizontal shear gives an instantaneous measure of the local deformations, in this case, prior to advection, while the Lyapunov exponent represents the integral deformation over the advection step. The vortex edge is identified by the strongest potential vorticity (PV) gradient with respect to equivalent latitude at the initial time [*Nash et al.*, 1996] (Figure 4, solid line).

[26] The vortex edge coincides well with the jet maximum, i.e., the minimum of the horizontal shear s_h. It also corresponds reasonably well to the minimum in the Lyapunov exponent λ. However, the correspondence of the vortex edge with the minimum in λ is not as clear cut as the correspondence with the minimum shear because the Lyapunov exponent is an integral quantity over the advection time step and so will reflect movements of the vortex edge over that time step. Studying Lagrangian evolution of material lines, *Pierce et al.* [1994] suggested that this zone may act as an effective kinematic barrier to large-scale mixing [*Randel et al.*, 1993; *Waugh et al.*, 1997].

[27] The results for one adaptive advection step with $\Delta t =$ 24 hours and $\lambda_c = 0.92$ days^{-1} are shown in Figure 5 (here λ_c is chosen to give reasonable results; the optimization of λ_c will be discussed in section 2.5). In Figure 5 (top) the new points that are inserted into the grid during the adaptation procedure after one time step are shown. Their color denotes the value of the corresponding Lyapunov exponent. The numerical diffusion D_+ calculated from (6) is shown in Figure 5 (bottom).

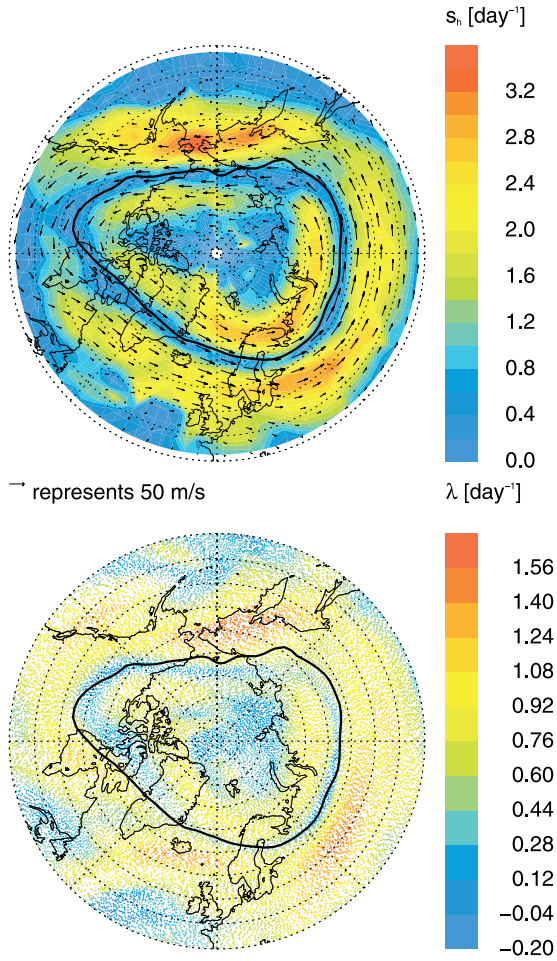

Figure 4. (top) Local shear rate derived from United Kingdom Meteorological Office (UKMO) horizontal winds (arrows) on 15 March 1997, 1200 UTC, at $\theta = 475$ K. Solid line denotes the edge of the polar vortex (see text for explanation). (bottom) Lyapunov exponent λ of each grid point, estimated from the deformation of the NN during the preceding advection step $\Delta t = 24$ hours.

[28] Comparing Figure 4 (bottom) with Figure 5 shows that (numerical) mixing is driven by the integral deformation rate measured in terms of the Lyapunov exponent λ and occurs in flow regions with $\lambda > \lambda_c$. Furthermore, because of the small values of the Lyapunov exponent at the vortex edge our dynamical adaptive gridding preserves the vortex edge mixing barrier. Thus, in contrast to the approach of *Fairlie et al.* [1999], a mixing barrier emerges as a natural consequence of linking mixing to integral deformation rate and requires no additional constraints.

[29] The strongest mixing occurs on the outer flanks of the jet stream and coincides with the largest Lyapunov exponents and shear rates (Figure 4). Inside the polar vortex a significant component of the shear is due to solid body rotation with respect to the pole. Thus, in such situations a mixing parameterization based directly on shear would introduce spurious mixing. Under the same circumstances our Lyapunov exponent based mixing parameterization has significantly smaller mixing rates (Figure 5, bottom). Nevertheless, the horizontal shear rate s_h shown in Figure

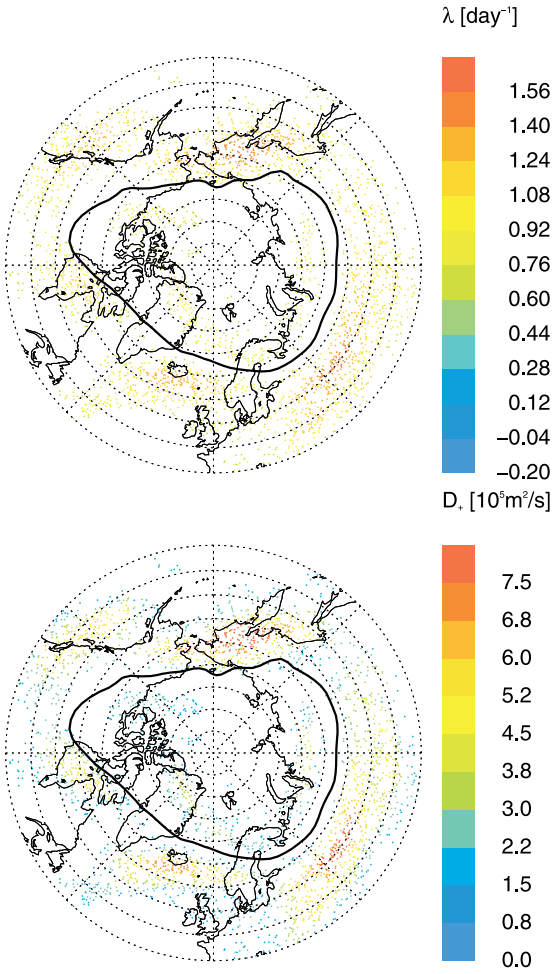

Figure 5. (top) New grid points (insertion and merging) resulting from the adaptation algorithm carried out for λ_c = 0.92 colored according to the corresponding Lyapunov exponents. Note that some new grid points have $\lambda < \lambda_c$. The existence of these points is a consequence of the deviation of the grid from a perfect uniformity at the beginning of the advection step (see Appendix B). (bottom) Equivalent diffusive mixing D_+ calculated from (6).

4, if compared, for example, with the strain rate s_t (not shown here), gives the best local (Eulerian) approximation of the integral deformation rate quantified in terms of λ.

[30] The idea that horizontal flow deformation may promote mixing is not new. *Aref* [1986] has postulated that large local deformation rates that are driven by stirring in the large-scale flow promote mixing across air-mass boundaries by increasing the air-mass interfacial area. This effect has been quantified using the idea of an effective diffusivity [*Nakamura*, 1996]. *Haynes and Shuckburgh* [2000] have shown that transport barriers such as the vortex edge or the subtropical jet are regions with small effective diffusivity.

[31] Summarizing, the dynamical adaptive gridding preserves not only the quasiuniform grid but, additionally, leads to an inhomogeneous (both in time and space) and anisotropic (i.e., dependent on the wind direction) mixing between APs. Given a grid resolution r_0 and a time step Δt, the mixing intensity is controlled by the critical Lyapunov exponent λ_c. In section 2.5 we show how the value of the Lyapunov exponent may be constrained by observations.

2.5. A Vortex Breakup Case Study: Implications for Mixing

[32] Most current satellite observations lack the high spatial resolution required to observe all but the largest filamentary structures in the atmosphere. An exception to this is the Cryogenic Infrared Spectrometers and Telescopes for the Atmosphere (CRISTA) instrument with 200-km horizontal and 2.5-km vertical resolution. CRISTA was first flown 3–14 November 1994, on the NASA space shuttle STS 66 [*Offermann et al.*, 1999] (version 3), so that it had a good chance to observe the southern vortex breakup. During this period the South Polar vortex had indeed begun to decay, with vortex fragments evident between ~700 and ~1300 K [*Manney et al.*, 1996]. An example of asynoptic observations of N_2O transformed to a central synoptic time is shown in Figure 6. The gradient of N_2O at the vortex edge over the southern Pacific and two areas of low N_2O mixing ratios between 20°S and 40°S (denoted as A and B in Figure 6) are evident on the 700-K potential temperature surface. These phenomena were consistently observed between 4 and 10 November (for the full study of this episode see P. Konopka et al. (Mixing intensity at the edge of the Southern Polar vortex deduced from CRISTA-1 experiment, submitted to *Journal of Atmospheric Sciences*, 2002).

[33] We simulated with CLaMS the isentropic transport of N_2O at 700 K and compared the results with CRISTA observations. Starting from an initial distribution on 20 October 1994 (Figure 7), two simulations were performed: a high-resolution simulation with ≈50,000 grid points, i.e., $r_0 \approx 60$ km, and a low-resolution simulation with ≈7000 grid points, i.e., $r_0 \approx 200$ km, uniformly distributed over the Southern Hemisphere. To determine the initial distribution,

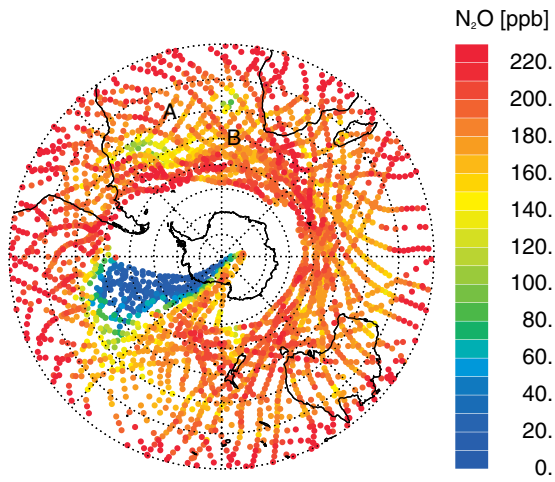

Figure 6. Synoptic map of N_2O mixing ratios measured during Cryogenic Infrared Spectrometers and Telescopes for the Atmosphere (CRISTA) flight on 10 November 1994, 1200 UCT, at θ = 700 K. Here the asynoptic profiles of N_2O (observed in a 24-hour window starting on 10 November 1200 UCT) were linearly interpolated to θ = 700 K and assimilated to a synoptic time using isentropic trajectories driven by UKMO winds (see part 2).

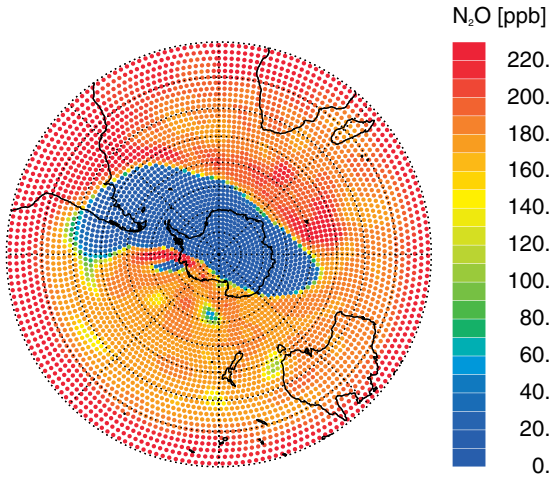

Figure 7. Initial N_2O distribution on 20 October 1994 at 700 K for the high-resolution CLaMS configuration with mean distance between grid points $r_0 \approx 60$ km. Initialization was determined from CRISTA observations by use of the PV-tracer correlation technique (see part 2).

a PV-N_2O correlation valid for 700 K was derived using observations between 4 and 6 November 1996 and the corresponding UKMO PV values. The evolution of N_2O mixing ratios during the simulation is characterized by filaments that are peeled off and wrapped around the vortex. The advection time step was chosen to be 12 hours and the critical Lyapunov exponent λ_c was chosen so that the simulated N_2O distributions are similar to the CRISTA observations.

[34] For the low-resolution simulation, three cases are shown in Figure 8 with zero (top panel), moderate (middle panel), and excessive mixing (bottom panel). Note that with a smaller value for λ_c, the separation criteria are more frequently satisfied and so mixing becomes more widespread. Thus, although the equivalent diffusivity along the flow D_+ decreases, the more important transverse equivalent diffusivity D_-, representing cross-gradient mixing, becomes more significant.

[35] Figure 9 shows results for $\lambda_c = 1.2$ days^{-1} and $r_0 = 60$ km. A value of $\lambda_c = 1.2$ days^{-1} implies that scale collapse and stretching by roughly a factor of 1.8 over 12 hours are permitted before the mixing procedure will be activated. Thus a fluid element with an intrinsic 2-D isentropic scale of 60 km would be stretched down to a 110-km long and 33-km wide filament before mixing sets in. These simulations with higher spatial resolution show significantly less mixing for the same value of λ_c than the corresponding low spatial resolution simulations due to the dependence of the separation criterion on r_0 (see (6)).

[36] An alternative isentropic transport simulation has been performed using Eulerian transport scheme designed to minimize numerical diffusion [*Prather*, 1986]. This version of the "Prather" scheme has been described by *Orsolini* [1995]. The results of a simulation carried out for the same time period and based on the same UKMO winds are shown in Figure 9 (bottom panel). The spatial resolution was chosen to be comparable to the CLaMS high-resolution case (1.125° in meridional and zonal direction). In the alternative Eulerian simulation the main vortex is clearly evident and, as with the CLaMS scheme, has the strongest N_2O gradients roughly where they have been observed by CRISTA. This version of the Prather scheme also clearly generates and preserves filaments down to a scale comparable to the underlying Eulerian grid. However, two main

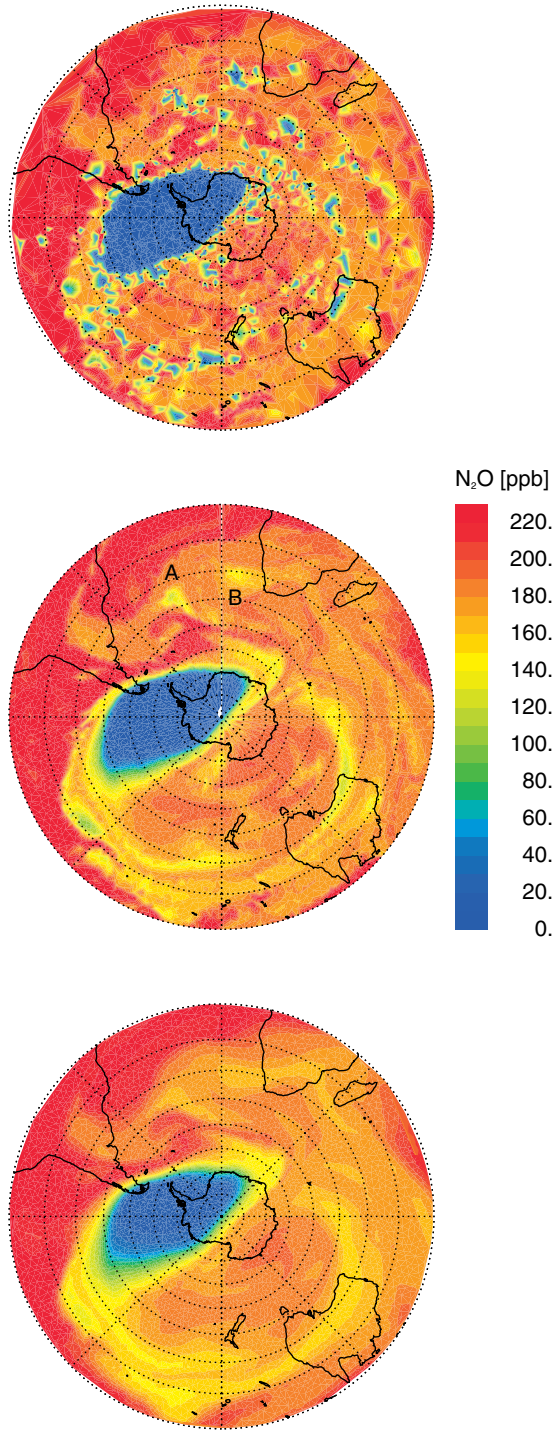

Figure 8. CLaMS results obtained with the low-resolution grid-point density ($r_0 \approx 200$ km) and $\Delta t = 12$ hours on 10 November at $\theta = 700$ K for different values of the Lyapunov exponent. (top) Pure advection $\lambda_c = \infty$, i.e., no adaptation. (middle) Moderate mixing, $\lambda_c = 1.2$ days^{-1}. (bottom) Excessive mixing, $\lambda_c = 0.6$ days^{-1}.

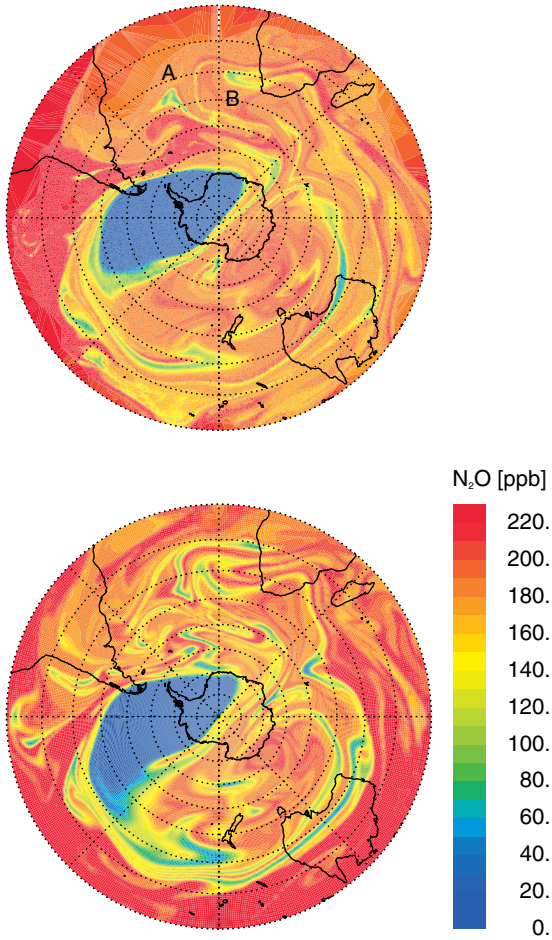

Figure 9. Lagrangian (CLaMS) versus Eulerian transport of N_2O compared on 10 November 1994 at $\theta = 700$. (top) CLaMS transport obtained with the high-resolution configuration $r_0 \approx 60$ km, $\Delta t = 12$ hours, and $\lambda_c = 1.2$ days^{-1}, slightly underestimating mixing. (bottom) Result of isentropic Eulerian transport employing the Prather scheme [*Prather*, 1986] with a comparable horizontal resolution.

deficiencies can be noted when compared to CRISTA observations: filamentation is more extensive, and the gradient of N_2O over the southern Pacific Ocean is less pronounced. Alternative versions of the Prather scheme exist that reduce some of these problems (M. J. Prather, private communication, 2000).

[37] By contrast, the high-resolution CLaMS simulations preserve the gradients in N_2O in a much more realistic manner, and although some filaments are present that are not evident in the CRISTA observation, their presence is much less pronounced. Furthermore, the two low-N_2O features A and B seen in the CRISTA observations that are advected around the vortex and finally into the southern Atlantic are well simulated and are not dissipated. Thus the critical Lyapunov exponent is optimized such that the features A and B are preserved and reasonably well simulated. However, with the chosen value of λ_c, some filaments are not dissipated, but persist in contrast to the observed N_2O distributions.

[38] The difference between the ClaMS simulated filaments and the features observed with CRISTA may be due to one factor or a combination of several factors: errors in the initialization, errors in the UKMO winds, and/or CRISTA resolving vertical scales of the order of 2.5 km, therefore leaving features of smaller vertical extent unresolved. However, as we have seen, small-scale features with sufficient vertical extent are clearly detected by CRISTA: the vertical range of the structures A and B amounts to ~6 km.

[39] In the CRISTA data the vertical scales are dominated by the vertical resolution (2.5 km). Consequently, it is only possible to optimize the Lyapunov exponent relative to the apparent atmospheric state, i.e., that observed by CRISTA. Thus the equivalent diffusivities that can be calculated from (6) may be considered as apparent diffusivities that overestimate the real atmospheric mixing owing to the "optical mixing" arising from the limited vertical resolution Δz of the CRISTA observations whereby features with a vertical extent below Δz would be smeared out.

3. Northern Winter/Spring Transition Simulation for 1997

[40] The 1997 Northern Hemisphere spring polar vortex was strong, cold, and circumpolar, in particular during the period from February into late April [*Coy et al.*, 1997]. Record low total ozone amounts were reported for this period [*Newman et al.*, 1997; *Pierce et al.*, 1997] that arose due to a combination of dynamical and chemical effects [e.g., *Müller et al.*, 1997; *Lefèvre et al.*, 1998]. For this period, to test CLaMS transport, we carried out long-lived tracer simulations for CH_4. In part 2, simulations of ozone loss for the same period will be described. We initialized CLaMS on 23 February 1997 on the 475 K isentropic surface and considered a time period of 44 days ending on 8 April. As in section 2.5, the same high- and low-resolution simulations will be considered.

[41] Using Halogen Occultation Experiment (HALOE) observations and a PV-tracer correlation technique (see part 2), an initial CH_4 mixing ratio distribution is determined. Net diabatic heating rate calculations at 475 K indicate that up until the beginning of March the air within the vortex descends with a rate of the order of 1 K day^{-1}.

[42] Thereafter, as the sun returns to high latitudes and polar bears awaken, calculations indicate that vortex air is below its equilibrium radiative temperature and furthermore that ascent rates of the order of 0.5 K day^{-1} will occur due to this solar heating. Calculations also indicate that relatively warm air masses originating from midlatitudes and tropical regions descend with a rate of the order of 1.0 K day^{-1} before being mixed into the outer vortex edge. Figure 10 shows the vertical position of ~50,000 APs on 15 March calculated in terms of diabatic trajectories. Large contrasts in vertical displacements of the APs at the vortex edge are evident, in accordance with *Schoeberl et al.* [1992]. The calculated net vertical displacements during the case study period do not exceed 30 K (≈1.5 km) for latitudes between 45°N and 90°N. As this vertical range is smaller than the vertical resolution (≈2.5 km) of the HALOE CH_4 observations used for initialization, it is reasonably well justified to invoke an isentropic approximation.

[43] Again, we compare the results for the isentropic CLaMS transport with the equivalent Eulerian simulation obtained with the Prather scheme (Figure 11). In contrast to

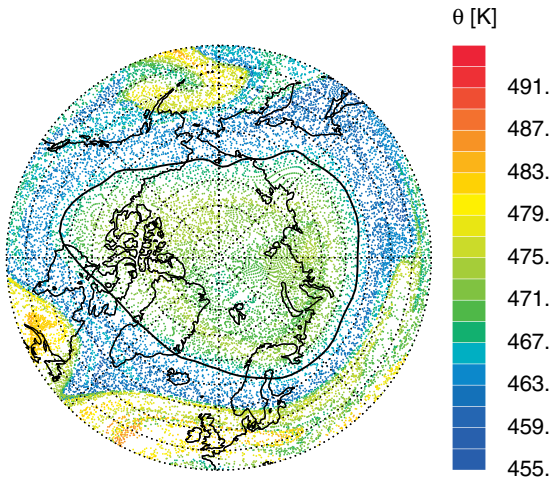

Figure 10. Potential temperature of air parcels on 15 March initialized on 23 February 1997 at 475 K, advected by UKMO winds and taking account of diabatic descent. At the vortex edge (solid line), large contrasts in vertical displacements of the air parcels are evident.

the CRISTA period, the spring period of 1997 was characterized by high vortex stability [*Coy et al.*, 1997] without pronounced filamentation. For this episode the results for all three simulations are more similar (Figure 12) than the previous CRISTA period simulations (Figure 9). The most pronounced differences relate to the vortex edge. The Prather scheme indicates a very sharp edge that coincides well with the vortex edge as diagnosed with the PV-gradient method, while both CLaMS simulations have a more gradual transition from outer to inner vortex methane values. Additionally, the high-resolution ClaMS simulation shows the penetration of outer vortex air deep into the vortex core. Thus clear differences exist between these two simulations that could be discriminated between experimentally. At this stage, no suitable analysis has been conducted that would distinguish between the results of the Lagrangian and Eulerian methodologies.

[44] To investigate the different behavior of the transported tracers during the CRISTA fall 1994 and spring 1997 period, we consider the statistics of the horizontal shear s_h derived from the horizontal UKMO winds for both studies. In Figure 12 the frequency distribution P for horizontal shear values s_h greater than a given value is shown. The results indicate that horizontal shear rates exceeding $s_h = 2\lambda_c = 2.4$ days^{-1} occur over >20% of the Southern Hemisphere during the CRISTA period, whereas horizontal shear rates exceeding $s_h = 2\lambda_c = 2.4$ days^{-1} occur over <5% of the Northern Hemisphere. Thus the Northern Hemisphere spring period 1997 is dominated by advection rather than mixing. Understandably then, the Prather and CLaMS transport schemes in Figure 11 show only small differences, with slightly more mixing at the vortex edge evident in the Lagrangian study.

4. Summary and Conclusions

[45] We have described a novel tracer transport scheme of a new stratospheric chemistry transport model (CLaMS) that relies on a Lagrangian rather than on a Eulerian formulation of the advection equation.

[46] We have shown that for a given simulation defined by the horizontal resolution r_0 and the length of the advection step Δt, a single critical parameter, the Lyapunov exponent λ_c, can be introduced that may be used as a criterion for the intensity of mixing in the model. This criterion leads to the definition of a heterogeneous and anisotropic equivalent diffusivity as a diagnostic tool to

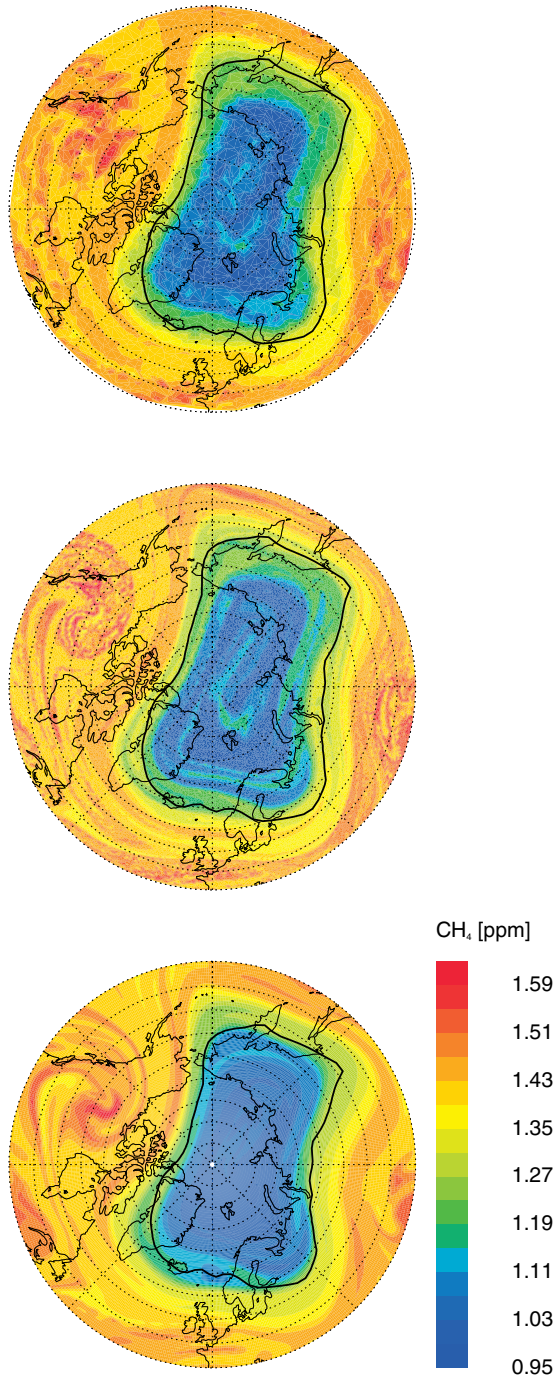

Figure 11. Lagrangian versus Eulerian isentropic transport of CH_4 for a time period of 44 days starting on 23 February and ending on 8 April 1997. (top) CLaMS with low-resolution configuration. (middle) CLaMS with high-resolution configuration. (bottom) Prather scheme with spatial resolution as in middle panel.

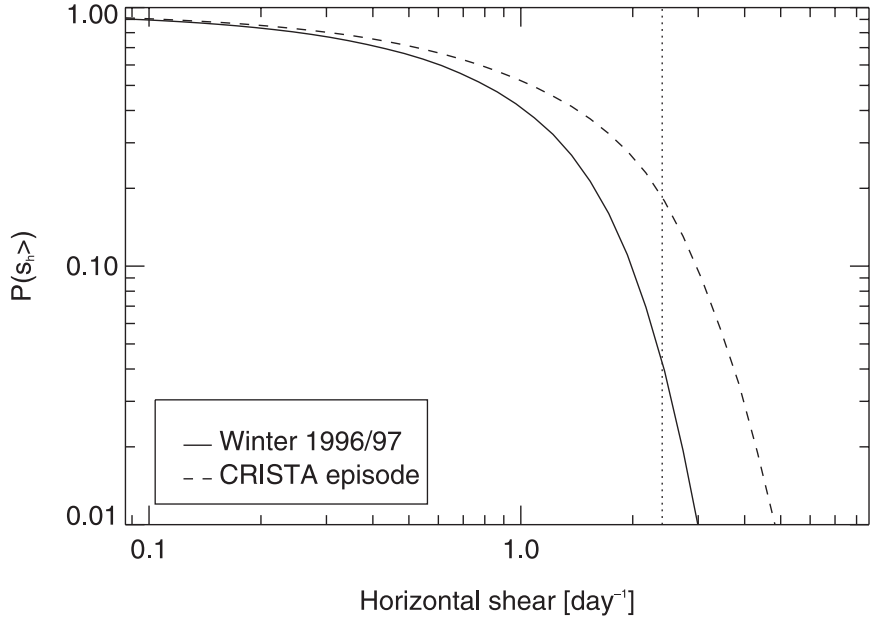

Figure 12. Shear frequency distribution calculated for the time period between 20 October and 10 November 1994 at 700 K in the Southern Hemisphere and between 23 February and 8 April 1997 at 475 K in the Northern Hemisphere. Shear value corresponding to the critical value $\lambda_c = 1.2$ days^{-1} is indicated by the dotted line at $2\lambda_c = s_h = 2.4$ days^{-1}.

quantify the intensity of mixing. The equivalent diffusivity, so calculated, indicates that mixing is limited across the model polar vortex edge. *Nakamura* [1996] came to a similar conclusion by considering the elongation rates of PV isopleths.

[47] The 2-D isentropic scheme presented here describes how an ensemble of APs is transported by model winds and regridded using a dynamically adaptive grid algorithm. Deformation of regions of the grid occurs and dynamical adaptive gridding is applied when the critical Lyapunov exponent has been exceeded. Consequently, the corresponding mixing is driven by the integral deformation of the large-scale flow over a time step Δt.

[48] The dichotomy between the numerical grid-point description and physical AP description of the dynamical adaptive grid procedure is illustrated in Figure 13. Interpreted as a flow-following grid, one may consider the adaptation procedure as introducing numerical diffusion, while considered as an ensemble of APs, the adaptation represents a mixing procedure. Because of coupling between

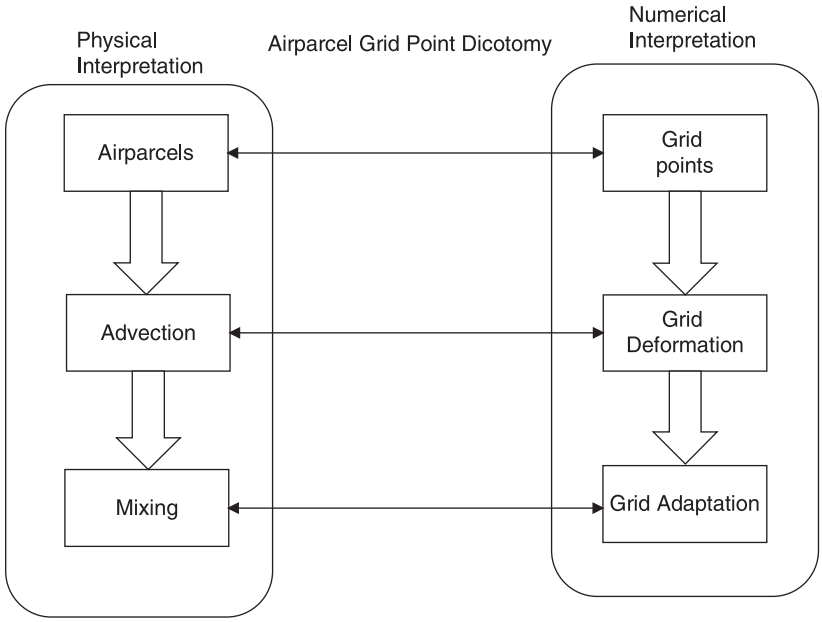

Figure 13. Dichotomy between the numerical grid point description and physical air parcel description.

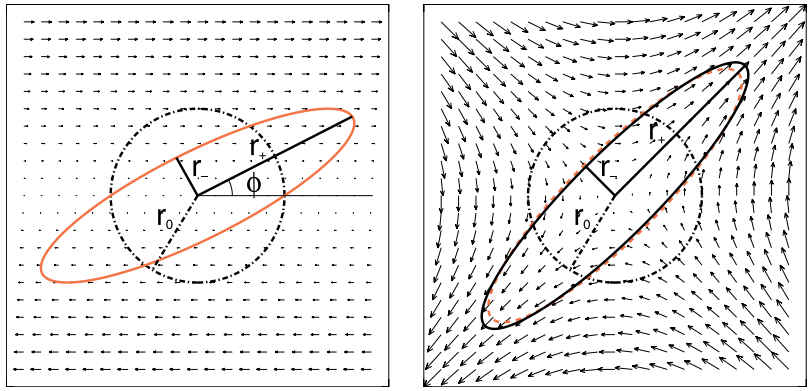

Figure A1. Deformation of a unit circle in a uniform shear (left) and strain (right) flow. With $s_h = s_t$ and the same value of the time step Δt, a circle with the radius r_0 is deformed into an ellipse (solid line) with minor and major axes $r_\pm$ given by the (4) (red) and (5) (black). Here ϕ describes the tilt angle in the shear case. For s_h given by (A4) both deformations are equal (red dashed line) up to a solid body rotation.

the integral deformation in the flow, adaptation of the grid, and mixing, the intensity of mixing depends on the deformation strength through the choice of the critical Lyapunov exponent λ_c. For sufficiently large values of λ_c the mixing is completely switched off; the transport reduces to a pure advection along the trajectories. One could make a similar philosophical distinction in a conventional grid-point advection scheme; however, the numerical diffusion, even when sometimes implicitly coupled to the flow deformation [see, e.g., *Rood*, 1987], cannot be explicitly controlled.

[49] One may consider the impacts of the forgoing procedure on two levels, either the dynamical adaptive grid or the APs associated with this grid. On the level of the dynamical adaptive grid, when the grid deforms and is then adapted, numerical diffusion is introduced at those grid points where adaptation occurs. Alternatively, if one considers the associated APs, when adaptation occurs, it leads to instantaneous mixing between APs.

[50] A comparison of CRISTA data with model simulations indicates that a value of $\lambda_c = 1.2$ days^{-1} gives reasonable results for a mixing case study of the Antarctic polar vortex. Significantly, studies of an undisturbed 1996–1997 spring Arctic vortex indicate that the same value of λ_c also gives reasonable results even during a situation with less pronounced mixing. This leads to the conjecture that it may be possible to define a range of critical Lyapunov exponents for which an appropriate mixing parameterization can be achieved. The implications of the transport algorithm described here for the simulation of the stratospheric chemistry are discussed in part 2 of this work.

Appendix A: Lyapunov Exponent in a Uniform Strain or Shear Flow

[51] Here we interpret the Lyapunov exponent λ describing the integral deformation in the flow in terms of the instantaneous flow properties such as local shear or strain that are usually used in the Eulerian approach. Consider two idealized flow configurations with the 2-D velocity fields given by

$$\mathbf{u}_{sh} := [s_h y, 0] \tag{A1}$$

$$\mathbf{u}_{st} := [s_t y/2, s_t x/2]. \tag{A2}$$

Equation (A1) describes a uniformly sheared flow with a shear rate s_h, and (A2) denotes a pure strain flow with a strain rate s_t (see Figure A1). Solving the ordinary differential equation $\dot{\mathbf{r}}(t) = \mathbf{u}$ with $\mathbf{r} = (x, y)$ and $\mathbf{r}(0) = \mathbf{r}_0 = (x_0, y_0)$, the general solution for the shear and strain flow can be written as $\mathbf{r} = \mathbf{A} \cdot \mathbf{r}_0$ with the matrix $\mathbf{A}$ given by [*Perko*, 1996]

$$\begin{aligned} \mathbf{A}_{sh} &= \begin{pmatrix} 1 & s_h t \\ 0 & 1 \end{pmatrix} \\ \mathbf{A}_{st} &= \frac{1}{2}\begin{pmatrix} 1 & 1 \\ 1 & -1 \end{pmatrix}\begin{pmatrix} \exp\left(\frac{1}{2}s_t t\right) & 0 \\ 0 & \exp\left(-\frac{1}{2}s_t t\right) \end{pmatrix}\begin{pmatrix} 1 & 1 \\ 1 & -1 \end{pmatrix} \end{aligned} \tag{A3}$$

for the shear and strain case, respectively. Transforming these explicit solutions into the principal axes, it can be shown that in both cases a circle with the radius r_0 is deformed into an ellipse with minor and major axes r_- and r_+. The r_- and r_+ are given by (4) and (5). Thus, in a constant strain flow the relation $\lambda = s_t/2$ holds, and the Lyapunov exponent scales with the strain rate.

[52] In addition, for a given shear value s_h a corresponding strain s_t can be determined with

$$\exp(s_t \Delta t) = 1 + s_h \Delta t \tan^{-1}\phi, \tag{A4}$$

so that a circle is deformed, up to a solid body rotation, in the same way. Furthermore, in the limit $s_h \Delta t \ll 1$ and $s_t \Delta t \ll 1$ both the shear- and strain-induced deformations (equations (4) and (5)) tend to the same linear form so that

$$\frac{r_\pm^2}{r_0^2} = 1 \pm s_h \Delta t = 1 \pm s_t \Delta t. \tag{A5}$$

Appendix B: Equivalent Diffusion of the Dynamical Adaptive Gridding

[53] Here we describe the details of the mixing intensity introduced by the DAG procedure, both in r space and in λ space, by taking into account (6). Especially in the r space, one can rewrite (6) as

$$D_\pm(r) \approx \begin{cases} 0 & r_-^c < r < r_+^c \\ D_0 (r/r_0)^2 & \text{elsewhere} \end{cases}, \tag{B1}$$

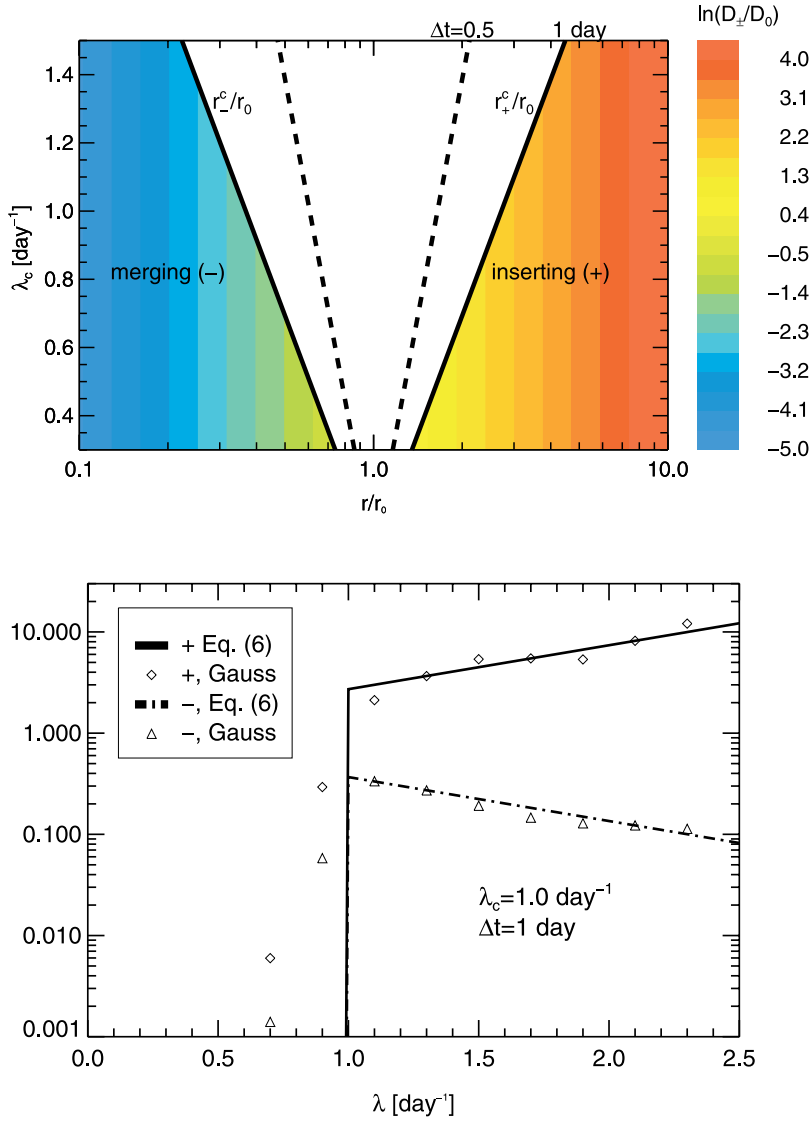

Figure A2. Numerical diffusion of the dynamical adaptive grid algorithm in the (top) r space and (bottom) λ space. In the r space the values of $D_{\pm}/D_0$ are calculated by use of (B1). The validity of the parameterization (equation (6)) in the λ space (solid and dashed lines in the bottom panel) is tested by the comparison with analytically known dispersion of Gaussian 2-D distribution (diamonds and triangles). With the exception of flow configurations with $0.7 < \lambda < \lambda_c = 1$ day^{-1}, (B2) approximates fairly well the numerical diffusion in a linearly sheared flow.

with $D_0 = r_0^2/4\Delta t$ and $r_{\pm}^c = r_0 \exp(\pm\lambda_c \Delta t)$. This relation is shown in Figure A2 (top panel), where the numerical diffusion due to merging (left-hand side of panel) and inserting grid points (right-hand side of panel) is plotted. Note that the r range where no mixing occurs (Figure A2, white region) strongly depends on the choice of the critical Lyapunov exponent λ_c and time step Δt.

[54] In addition, mixing in the λ space can only be understood in a statistical way. Here we write (6) as

$$D_{\pm}(\lambda) \approx \frac{r_{\pm}^2}{4\Delta t} = D_0 \begin{cases} \exp(\pm 2\lambda \Delta t) & \lambda \geq \lambda_c \\ 0 & \lambda < \lambda_c. \end{cases} \qquad \text{(B2)}$$

Thus mixing occurs if $\lambda > \lambda_c$ with the intensity dependent on the distances between all the APs satisfying the mixing criterion in the r space. To check the validity of (6) for a suitable range of the grid and time step values, analytical solutions for advection and diffusion of Gaussian 2-D distributions in an idealized linearly sheared flow are used. In particular, we consider the dispersion of a Gaussian tracer distribution due to dynamical adaptive gridding in an idealized linearly sheared flow. The equivalent diffusion parameters can be estimated by comparing the simulated tracer dispersion with corresponding analytical solutions for dispersion of a 2-D Gaussian tracer distribution [*Konopka*, 1995]. The results of this procedure for $\lambda_c = 1$ day^{-1} are shown in Figure A2, where values for $D_{\pm}/D_0$ ($D_0 = r_0^2/4\Delta t$) derived from comparison with analytical solutions for different values of λ are plotted as diamonds and triangles. In addition, the idealized form of (6) is also shown in Figure A2 (solid and dashed lines).

[55] Comparison of the results obtained analytically with (B2) shows good agreement for $\lambda \geq \lambda_c$. Small differences occur for flow configurations with $0.7 < \lambda < \lambda_c$, i.e., the cliff at $\lambda = \lambda_c$ described by (B2) is steeper than tracer dispersion derived from comparison with the analytical Gaussian solutions. In the algorithm as implemented, the transition will not be as sharp, since some APs will mix even though the critical Lyapunov exponent has not been exceeded, when the initial separation is different from the mean separation distance ($r < r_0$ or $r > r_0$) but one of the separation criteria ($r < r_c^-$ or $r > r_c^+$) is satisfied.

[56] In conclusion, (6) reasonably approximates the mixing intensity for horizontal grid resolutions r_0 and time steps Δt varying between 50 and 500 km and 6 and 24 hours, respectively.

[57] **Acknowledgments.** We are grateful for the contributions of K. Shine, J. Haigh, and W. Zhong, who provided us with radiation codes. We thank M. Bithell for sharing with us his experience on the adaptive grids. R. Swinbank provided us with the trajectory model, and P. Simon provided us the Prather scheme. The authors thank Jürgen Ankenbrand and Nicole Thomas for their programming support. We thank UKMO for meteorological analysis. This research was supported by the German Bundesministerium für Bildung, Wissenschaft, Forschung und Technologie (BMBF) within the project "Ozonforschungsprogramm" (contract 01 LO 9525/0).

References

Appenzeller, C., H. C. Davies, and W. A. Norton, Fragmentation of stratospheric intrusions, *J. Geophys. Res.*, *101*, 1435–1456, 1996.

Aref, H., Chaotic advection in Stokes flow, *Phys. Fluids*, *29*, 3515–3521, 1986.

Austin, J., Lagrangian photochemical modeling studies of the 1987 Antarctic spring vortex, 2, Seasonal trends in ozone, *J. Geophys. Res.*, *94*, 16,717–16,735, 1989.

Balluch, M. G., and P. H. Haynes, Quantification of lower stratospheric mixing processes using aircraft data, *J. Geophys. Res.*, *102*, 23,487–23,504, 1997.

Barber, C. B., P. D. David, and H. Huhdanpaa, The quickhull algorithm for convex hulls, *Trans. Math. Software*, *22*, 469–483, 1996.

Collins, W. J., D. S. Stevenson, C. E. Johnson, and R. G. Derwent, Tropospheric ozone in a global-scale three-dimensional Lagrangian model and its response to NO_x emission controls, *J. Atmos. Chem.*, *26*, 223–274, 1997.

Coy, L., E. Nash, and P. Newman, Meteorology of the polar vortex: Spring 1997, *Geophys. Res. Lett.*, *24*, 2693–2696, 1997.

Dritschel, D. G., Contour dynamics and contour surgery: Numerical algorithm for extended, high-resolution modeling of vortex dynamics in two-dimensional, inviscid, incompressible flows, *Comput. Phys. Rep.*, *10*, 77–146, 1989.

Edouard, S., B. Legras, F. Lefèvre, and R. Eymard, The effect of small-scale inhomogeneities on ozone depletion in the Arctic, *Nature*, *384*, 444–447, 1996.

Fairlie, T. D., R. B. Pierce, J. A. Al-Saadi, W. L. Grose, J. M. Russell, M. H. Proffitt, and C. R. Webster, The contribution of mixing in Lagrangian photochemical predictions of polar ozone loss over the Arctic in summer 1997, *J. Geophys. Res.*, *104*, 26,597–26,609, 1999.

Geist, K., U. Parlitz, and W. Lauterborn, Comparison of different methods for computing Lyapunov exponents, *Prog. Theor. Phys.*, *83*, 875–893, 1990.

Haynes, P., and E. Shuckburgh, Effective diffusivity as a diagnostic of atmospheric transport, 1, stratosphere, *J. Geophys. Res.*, *105*, 22,777–22,794, 2000.

Konopka, P., Analytical Gaussian solutions for anisotropic diffusion in a linear shear flow, *J. Non Equilib. Thermodyn.*, *20*, 78–91, 1995.

Lefèvre, F., F. Figarol, K. S. Carslaw, and T. Peter, The 1997 Arctic ozone depletion quantified from three-dimensional model simulations, *Geophys. Res. Lett.*, *25*, 2425–2428, 1998.

Lorenz, E. N., Deterministic non-periodic flow, *J. Atmos. Sci.*, *20*, 130–141, 1963.

Lutman, E. R., J. A. Pyle, R. L. Jones, D. J. Lary, A. R. MacKenzie, I. Kilbane-Dawe, N. Larsen, and B. Knudsen, Trajectory model studies of ClO_x activation during the 1991/92 Northern Hemispheric winter, *Geophys. Res. Lett.*, *21*, 1419–1422, 1994.

Lutman, E. R., J. A. Pyle, M. P. Chipperfield, D. J. Lary, I. Kilbane-Dawe, J. W. Waters, and N. Larsen, Three-dimensional studies of the 1991/1992 Northern Hemisphere winter using domain-filling trajectories with chemistry, *J. Geophys. Res.*, *102*, 1479–1488, 1997.

Manney, G. L., R. Swinbank, and A. O'Neill, Stratospheric meteorological conditions from the November 3–12, 1994, ATMOS/ATLAS 3 measurements, *Geophys. Res. Lett.*, *23*, 2409–2412, 1996.

McIntyre, M. E., and T. N. Palmer, Breaking planetary waves in the stratosphere, *Nature*, *305*, 593–600, 1983.

McKenna, D. S., J. U. Grooß, G. Günther, P. Konopka, R. Müller, and G. Carver, A new Chemical Lagrangian Model of the Stratosphere (CLaMS), 2, Formulation of chemistry scheme and initialization, *J. Geophys. Res.*, *107*, 10.1029/2000JD000113, in press, 2002.

Morcrette, J.-J., Radiation and cloud radiative properties in the European Centre for Medium-Range Weather Forecasts forecasting system, *J. Geophys. Res.*, *96*, 9121–9132, 1991.

Morris, G. A., et al., Trajectory mapping and applications to data from the Upper Atmosphere Research Satellite, *J. Geophys. Res.*, *100*, 16,491–16,505, 1995.

Müller, R., J.-U. Grooß, D. McKenna, P. J. Crutzen, C. Brühl, J. M. Russell, and A. F. Tuck, HALOE observations of the vertical structure of chemical ozone depletion in the Arctic vortex during winter and early spring 1996–1997, *Geophys. Res. Lett.*, *24*, 2717–2720, 1997.

Nakamura, N., Two-dimensional mixing, edge formation, and permeability diagnosed in area coordinates, *J. Atmos Sci.*, *53*, 1524–1537, 1996.

Nash, E. R., P. A. Newman, J. E. Rosenfield, and M. R. Schoeberl, An objective determination of the polar vortex using Ertel's potential vorticity, *J. Geophys. Res.*, *101*, 9471–9478, 1996.

Newman, P., F. Gleason, R. McPeters, and R. Stolarski, Anomalously low ozone over the Arctic, *Geophys. Res. Lett.*, *24*, 2689–2692, 1997.

Ngan, K., and T. G. Shepherd, A closer look at chaotic advection in the stratosphere, I, Geometric structure, *J. Atmos. Sci.*, *56*, 4134–4152, 1999a.

Ngan, K., and T. G. Shepherd, A closer look at chaotic advection in the stratosphere, II, Statistical diagnostics, *J. Atmos. Sci.*, *56*, 4153–4166, 1999b.

Norton, W. A., Breaking Rossby waves in a model stratosphere diagnosed by a vortex-following coordinate system and a technique for advecting material contours, *J. Atmos. Sci.*, *51*, 654–673, 1994.

Offermann, D., K.-U. Grossmann, P. Barthol, P. Knieling, M. Riese, and R. Trant, Cryogenic Infrared Spectrometers and Telescopes for the Atmosphere (CRISTA) experiment and middle atmosphere variability, *J. Geophys. Res.*, *104*, 16,311–16,325, 1999.

Orsolini, Y. J., On the formation of ozone laminae at the edge of the Arctic polar vortex, *Q. J. R. Meteorol. Soc.*, *121*, 1923–1941, 1995.

Orsolini, Y. J., G. L. Manney, A. Angel, J. Ovarlez, C. Claud, and L. Coy, Layering in stratospheric profiles of long-lived trace species: Balloonborne observations and modeling, *J. Geophys. Res.*, *103*, 5815–5825, 1998.

Perko, L., *Differential Equations and Dynamical Systems*, Springer-Verlag, New York, 1996.

Pierce, R. B., T. D. Fairlie, W. L. Grose, R. Swinbank, and A. O'Neill, Mixing processes within the polar night jet, *J. Atmos. Sci.*, *20*, 2957–2972, 1994.

Pierce, R. B., J.-U. Grooß, W. L. Grose, J. M. Russell III, P. J. Crutzen, T. D. Fairlie, and G. Lingenfelser, Photochemical calculations along air mass trajectories during ASHOE/MAESA, *J. Geophys. Res.*, *102*, 13,153–13,167, 1997.

Pierce, R. B., J. A. Al-Saadi, T. D. Fairlie, J. R. Olson, R. S. Eckman, G. S. Lingenfelser, W. L. Grose, and J. M. Russell, Large-scale stratospheric ozone photochemistry and transport during the POLARIS campaign, *J. Geophys. Res.*, *104*, 26,525–26,545, 1999.

Plumb, R. A., D. W. Waugh, R. J. Atkinson, P. A. Newman, L. R. Lait, M. R. Schoeberl, E. V. Browell, A. J. Simmons, and M. Loewenstein, Intrusions into the lower stratospheric Arctic vortex during the winter of 1991–1992, *J. Geophys. Res.*, *99*, 1089–1105, 1994.

Prather, M. J., Numerical advection by conservation of second-order moments, *J. Geophys. Res.*, *91*, 6671–6681, 1986.

Preparata, F. P., and M. Shamos, *Computational Geometry: An Introduction*, Springer-Verlag, New York, 1985.

Randel, W. J., J. C. Gille, A. E. Roche, J. B. Kumer, J. L. Mergenthaler, J. W. Waters, E. F. Fishbein, and W. A. Lahoz, Stratospheric transport from the tropics to middle latitudes by planetary-wave mixing, *Nature*, *365*, 533–535, 1993.

Riese, M., X. Tie, G. Brasseur, and D. Offermann, Three-dimensional simulation of stratospheric trace gas distributions measured by CRISTA, *J. Geophys. Res.*, *104*, 16,419–16,435, 1999.

Rood, R. B., Numerical advection algorithms and their role in atmospheric transport and chemistry models, *Rev. Geophys.*, *25*(1), 71–100, 1987.

Schoeberl, M. R., L. R. Lait, P. A. Newman, and J. E. Rosenfield, The structure of the polar vortex, *J. Geophys. Res.*, *97*, 7859–7882, 1992.

Searle, K. R., M. P. Chipperfield, S. Bekki, and J. A. Pyle, Impact of spatial averaging on calculated polar ozone loss, 1, Model experiments, *J. Geophys. Res.*, *103*, 25,397–25,408, 1998a.

Searle, K. R., M. P. Chipperfield, S. Bekki, and J. A. Pyle, Impact of spatial averaging on calculated polar ozone loss, 2, Theoretical analysis, *J. Geophys. Res.*, *103*, 25,409–25,416, 1998b.

Sutton, R. T., H. Maclean, R. Swinbank, A. O'Neill, and F. W. Taylor, High-resolution stratospheric tracer fields estimated from satellite observations using Lagrangian trajectory calculations, *J. Atmos. Sci.*, *51*, 2995–3005, 1994.

Tan, D. G. H., P. H. Haynes, A. R. MacKenzie, and J. A. Pyle, Effects of fluid-dynamical stirring and mixing on the deactivation of stratospheric chlorine, *J. Geophys. Res.*, *103*, 1585–1605, 1998.

Tuck, A. F., R. T. Watson, E. P. Condon, and J. J. M. O. B. Toon, Planning and execution of ER-2 and DC-8 aircraft flights over Antarctica, August and September 1987, *J. Geophys. Res.*, *94*, 11,181–11,222, 1989.

Waugh, D. W., and R. A. Plumb, Contour advection with surgery: A technique for investigating finescale structure in tracer transport, *J. Atmos. Sci.*, *51*, 530–540, 1994.

Waugh, D. W., et al., Mixing of polar vortex air into middle latitudes as revealed by tracer-tracer scatterplots, *J. Geophys. Res.*, *102*, 13,119–13,134, 1997.

Woodman, R. F., and P. K. Rastogi, Evaluation of effective eddy diffusivity coefficients using radar observations of turbulence in the stratosphere, *Geophys. Res. Lett.*, *11*, 243–246, 1984.

Zhong, W., and J. D. Haigh, Improved broadband emissivity parameterization for water vapor cooling rate calculations, *J. Atmos. Sci.*, *52*, 124–138, 1995.

J.-U. Grooß, G. Günther, P. Konopka, D. S. McKenna, and R. Müller, Institute for Stratospheric Chemistry (ICG-1), Forschungszentrum Jülich, D-52425 Jülich, Germany. (j.-u.grooss@fz-juelich.de; g.guenther@fz-juelich.de; p.konopka@fz-juelich.de; danny@ucar.edu; ro.mueller@fz-juelich.de)

D. Offermann, Department of Physics, University of Wuppertal, D-42097 Wuppertal, Germany. (offerm@wpos2.physik.uni-wuppertal.de)

Y. Orsolini, Norwegian Institute for Air Research (NILU), Instituttveien 18, PO Box 100, N-2007 Kjeller, Norway. (orsilini@nilu.no)

R. Spang, EOS Space Research Center, University of Leicester, Leicester LEI 7RH, England, UK. (r.spang@le.ac.uk)